International Journal of Minerals, Metallurgy and Materials
Volume 26, Number 2, February 2019, Page 251
https://doi.org/10.1007/s12613-019-1730-z

Weldability and liquation cracking behavior of ZhS6U superalloy during electron-beam welding

Arash Khakzadshahandashti[1)], *Mohammad Reza Rahimipour*[1)], *Kourosh Shirvani*[2)], *and Mansour Razavi*[1)]

1) Department of Ceramic, Materials and Energy Research Center, Karaj 31787316, Iran

2) Department of Material and Renewal Energy, Iranian Research Organization for Science and Technology (IROST), Tehran 33535111, Iran

(Received: 19 April 2018; revised: 18 July 2018; accepted: 30 July 2018)

Abstract: The weldability of the ZhS6U nickel-based superalloy, which is prone to solidification cracking during electron-beam welding (EBW) repair processes, was investigated. The effects of two different pre-weld heat-treatment cycles on the final microstructure before and after welding were examined. Welds were made on flat coupons using an EBW machine, and the two heat-treatment cycles were designed to reduce γ′ liquation before welding. Microstructural features were also examined by optical and scanning electron microscopy. The results showed that the change in the morphology and size of the γ′ precipitates in the pre-weld heat-treatment cycles changed the ability of the superalloy to release the tensile stresses caused by the matrix phase cooling after EBW. The high hardness in the welded coupons subjected to the first heat-treatment cycle resulted in greater resistance to stress release by the base alloy, and the concentration of stress in the base metal caused liquation cracks in the heat-affected zone and solidification cracks in the weld area.

Keywords: weldability; ZhS6U superalloy; electron beam welding; heat-affected zone; liquation cracking; pre-weld heat treatment

1. Introduction

ZhS6U nickel-based casting superalloys are widely used in vanes and blades in the hot section of powerful land-based and aircraft gas turbine engines because of their excellent microstructural stability, outstanding high-temperature strength, and good hot corrosion resistance [1–4]. The high manufacturing cost and economic consequences of in-service damage often make the repair of damaged components desirable. Processes such as welding are suitable for the cost-effective repair of damaged parts [3,5].

Fusion welding is generally used to repair superalloy components; however, these alloys have limited weldability because defects introduced by welding and by post-welding heat-treatments render the components sensitive to heat-affected zone (HAZ) cracking [6]. One cause of HAZ cracking is the competition between mechanical driving forces for cracking (stress/strain generation) due to cooling stresses and the intrinsic resistance of the material to cracking along the grain boundaries [7]. The formation of weld liquation cracks is associated with the presence of a continuous or semi-continuous intergranular thin liquid film on HAZ grain boundaries. Tensile stresses induced during the weld thermal cycle are responsible for decohesion of the solid–liquid interface along grain boundaries [8–12]. It was reported that the formation of the γ′ phase through rapid re-precipitation induces large shrinkage stresses along with substantial intragranular strengthening. Accordingly, the factors that generally influence HAZ cracking are grain-boundary liquation, the amount of γ′ precipitates formed, the grain size, and the magnitude of the thermally induced stresses [5–6].

Compared with other welding techniques, electron-beam welding (EBW) is an attractive route for joining and repairing high-temperature materials because of its ability to join with good weld properties. It creates full-penetration welds in thick sections with a high depth-to-width ratio, and the welds can be formed in a single pass and with minor heat input. The very low heat input results not only in low distortion and residual stresses but also in good fatigue and

Corresponding author: Mohammad Reza Rahimipour E-mail: m-rahimi@merc.ac.ir

© University of Science and Technology Beijing and Springer-Verlag GmbH Germany, part of Springer Nature 2019

stress-corrosion properties [13].

The ZhS6U superalloy includes a high percentage of reinforced grain-boundary elements such as tungsten (approximately 10wt%–11wt%) and high percentages of aluminum and titanium as the constituents of the γ′-Ni_3(Al,Ti)-reinforced phase (totaling 7wt%). Thus, the ZhS6U superalloy microstructure is mostly composed of γ′ and carbide phases. Therefore, according to the weldability diagram of superalloys, it is highly sensitive to crack formation and the formation of unwanted phases after welding [14].

On the basis of the aforementioned literature, we designed experiments in the present work with the objective of improving the mechanical and metallurgical properties of ZhS6U weldments by using a pre-heat treatment to minimize intergranular liquation and HAZ cracking during EBW. To improve the weldability of ZhS6U by reducing the HAZ liquation cracking, the pre-weld microstructure and chemical distribution are controlled through a pre-heat treatment. The pre-weld heat-treatment cycles used in this study were based on suitable and acceptable pre-weld heat-treatment cycles reported in a previous investigation of the weldability of other superalloys [3]. In the present study, we modified the heat-treatment cycles reported previously because the γ′ solution annealing temperature of ZhS6U superalloy differs from those of other superalloys.

2. Experimental

Table 1 shows the chemical composition of the ZhS6U superalloy used in this research, as determined by X-ray fluorescence analysis.

Table 1. Chemical composition of the ZhS6U base metal wt%

Zr	C	Nb	Ti	Al	W	Mo	Co	Cr	Ni
0.05	0.15	0.95	2	5	10.34	1.59	9.47	8.68	Bal.

Coupons with dimensions of 30 mm × 10 mm × 3 mm were cut from the flat parts of a service-exposed vane, machined using a wire cutter, and then cleaned with acetone. Two heat-treatment cycles were designed to reduce γ′ liquation before welding: the first cycle was 1140°C/2 h/furnace cooling + 1050°C/16 h/water quenching, and the second cycle was (1140°C/2 h/furnace cooling + 1050°C/16 h/furnace cooling). All coupons were heat treated under argon shielding gas in an electrical tube furnace. The test samples were heated at 5°C/min. The furnace cooling of each cycle was also carried under argon gas.

After the samples were polished and cleaned, welds were made on coupons using an EBW machine. The welding current was varied from 2 to 3 mA at a constant voltage of 150 kV. The focusing current was considered constant. Because the samples were small, the specimens could not move against the electron beam; thus, the welded bead was created in the form of a spot with a 10 mm × 10 mm cross section. Under these parameters and conditions, full-penetration welds were obtained. Each welded coupon for characterization was cut into three cross sections using an abrasive cutting machine after the first and second heat-treatment cycles.

To investigate the microstructure, cut coupons after surface preparation (sanding and polishing) were electrolytically etched with a 10wt% oxalic acid solution for observation of the microstructure by optical microscopy (Olympus GX-71) and scanning electron microscopy (SEM; TESCAN VEGA-XMU). The optical and electron microscopy images of the microstructure were also analyzed with the Image J analysis software.

The hardness of the welded coupons was measured using the Vickers hardness test method after the heat treatment with different cycles and before welding. The Vickers hardness tests were performed under a load of 196 N in accordance with standard ASTM E92.

3. Results and discussion

3.1. Pre-weld microstructure

Fig. 1 shows optical microscopy and SEM images of the coupon without any pre-weld heat treatment of the service-exposed superalloy. The microstructure with an equiaxed grain structure is generally composed of three parts: a matrix phase (γ phase and γ′ precipitates), a γ–γ′ eutectic phase, and a coarse, needle-shaped, sometimes block-shaped carbide phase. According to the visual analysis software, the average size of the γ′ precipitates was 0.55 μm after the specimen's conventional service time.

Fig. 2 illustrates a non-heat-treated microstructure coupon in which the light phase and the needle-shaped carbide in the matrix phase (γ phase and γ′ precipitates, respectively) are visible. The energy dispersive spectroscopy (EDS) analysis results for point A (Fig. 2) are presented in Table 2. These results indicate that MC carbides are present in the microstructure. During the service time of the superalloy under high temperature, these carbides did not transform to $M_{23}C_6$ and M_6C carbides.

The aforementioned microstructural components with equiaxed grain structures are clearly visible in the heat-treated coupon in the first cycle (Fig. 3(a)) and the second cycle

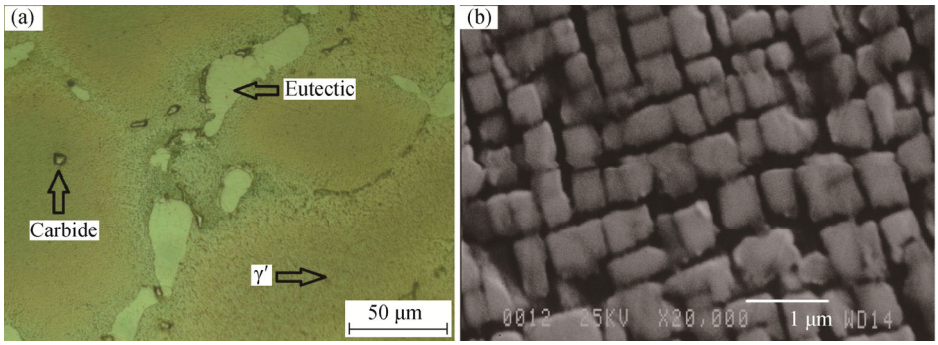

Fig. 1. Optical microscopic image (a) and SEM image (b) of the service-exposed superalloy without a pre-weld heat treatment.

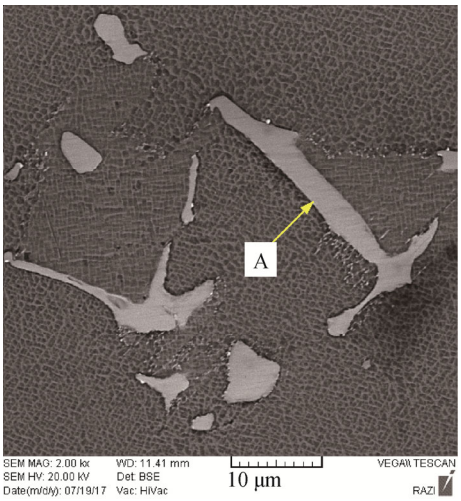

Fig. 2. MC carbide in the microstructure of the service-exposed superalloy sample.

Table 2. EDS analysis results corresponding to point A in Fig. 2 at%

C	Nb	Ti	W	Mo	Co	Cr	Ni
36.5	11.3	28.2	10.2	3.5	1.00	2.4	6.9

(Fig. 3(b)). A larger grain size and coarse microstructure components are observed in the microstructure of the service-exposed superalloy (Fig. 1(a)) compared with the microstructure of the coupon subjected to the first heat-treatment cycle (Fig. 3(a)). Grain coarsening of the eutectic and carbide phases is observed. Creep cavities are visible in the microstructure of the service-exposed superalloy (Fig. 1), which are created through its service operation. These microstructural changes during service will reduce creep resistance and the service life of the part. However, the microstructural components of the specimen subjected to the second heat treatment are slightly coarser than those of the specimen subjected to the first treatment because of the difference in cooling rates at the end of the two cycles [15].

Figs. 4 and 5 show SEM images of the microstructures of the sample coupons subjected to the first and the second heat-treatment cycles, respectively. Three general sections of the microstructure, including the matrix phase (γ phase and γ′ precipitates), γ–γ′ eutectic phase, and coarse, needle-shaped carbide phase, are visible in these images. Morphological changes and coarsening of the γ′ precipitates of the coupons subjected to the first and the second heat-treatment cycles were observed compared with the morphology and γ′ precipitates of the service-exposed superalloy. The γ′ precipitates were converted from cubic to spherical shapes with an average diameter of 0.74 μm after the heat treatment in the first cycle and an average diameter of 0.86 μm after the second heat-treatment cycle.

The microstructure of the coupon subjected to the second heat-treatment cycle is shown in Fig. 6. This image shows

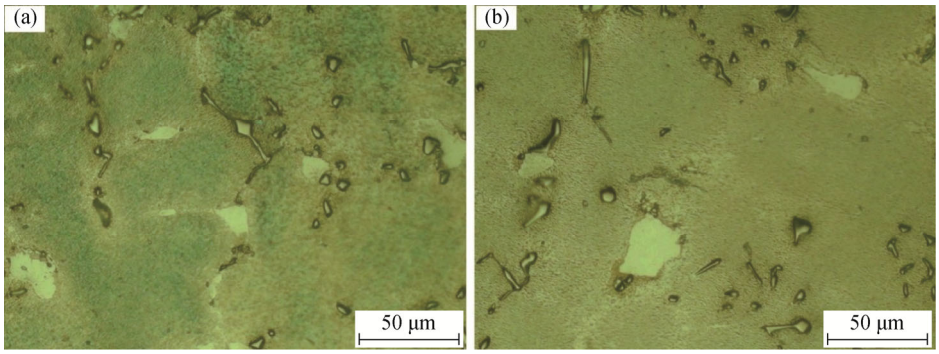

Fig. 3. Optical microstructure images of coupons subjected to the first heat-treatment cycle (a) and the second heat-treatment cycle (b).

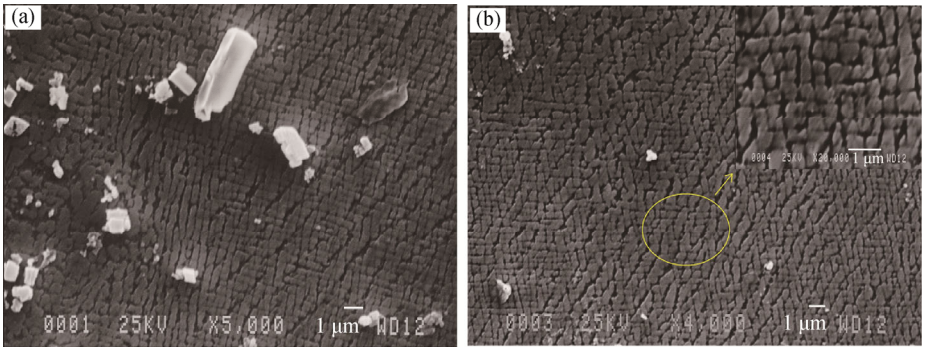

Fig. 4. Microstructure of the coupons subjected to the first heat-treatment cycle at different magnifications.

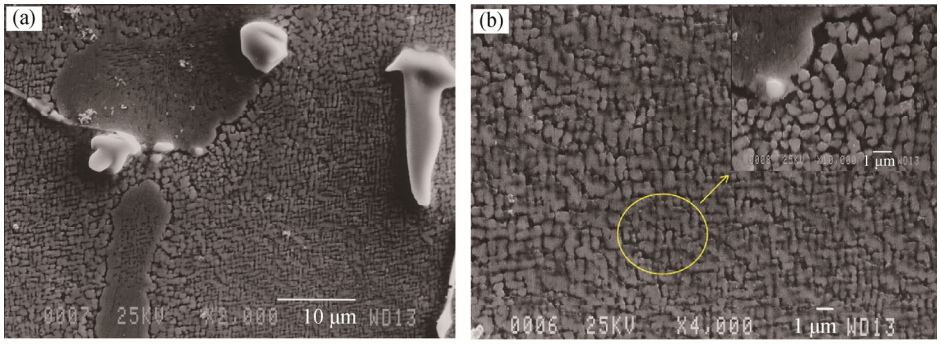

Fig. 5. Microstructure of the coupon subjected to the second heat-treatment cycle at different magnifications.

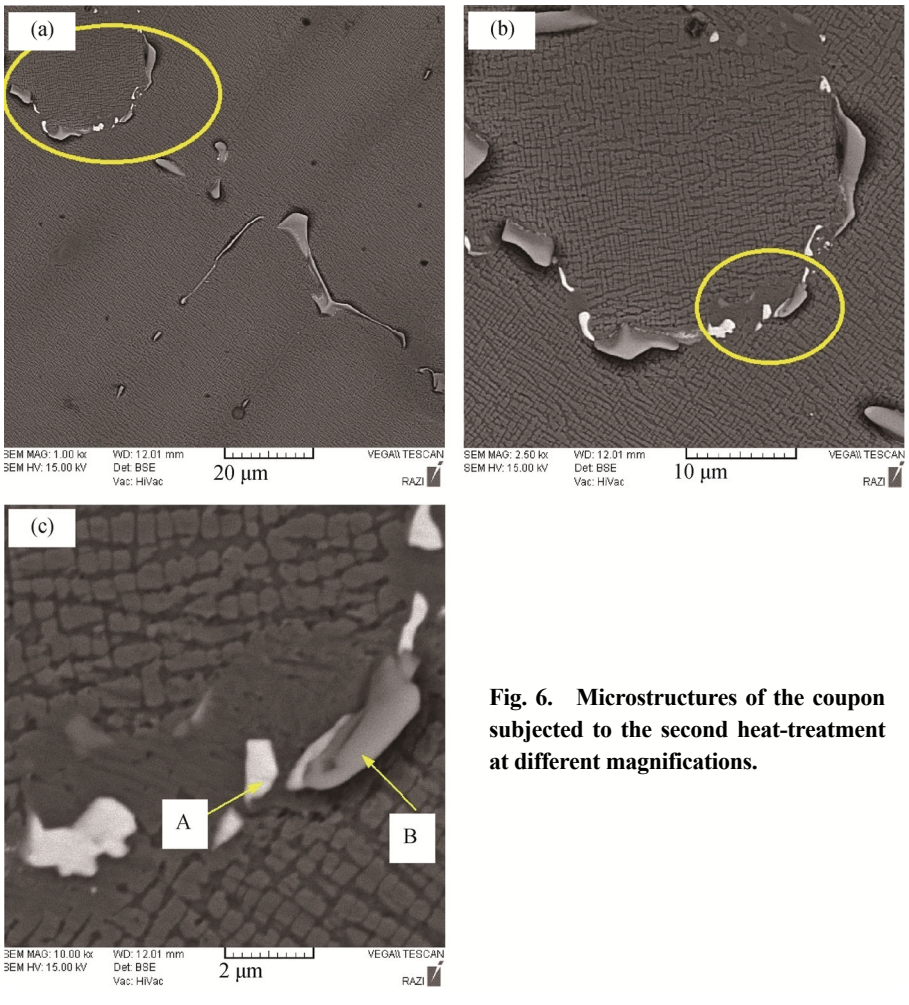

Fig. 6. Microstructures of the coupon subjected to the second heat-treatment at different magnifications.

carbides that formed as deposits alongside the boundaries and strengthened the boundary. Two types of carbides (MC and M_6C) are observed among the microstructures of the ZhS6U superalloy (Fig. 6(a)), as indicated by the yellow circle; this region is shown at higher magnification in Figs. 6(b) and 6(c). The EDS analysis results corresponding to points A and B (Table 3) confirm the combined composition of these two carbides. According to the EDS analysis results, point A, which isc related to the M_6C carbide, exhibits a brighter color than the MC carbide. The M_6C carbide is formed during the heat treatment by the following reaction [15]:

$$MC + \gamma \rightarrow M_6C + \gamma' \quad (1)$$

Table 3. EDS analysis results corresponding to points A and B in Fig. 6(c) at%

Point	C	Nb	Ti	W	Mo	Co	Cr	Ni
A	12.2	2.9	2.9	15.1	7.1	11.6	16.6	31.6
B	37.4	10.8	31.1	6.1	2.3	0.5	1.8	10.0

Fig. 7 shows the hardness variation of the coupons and the particle size of the γ′-phase precipitates after the first and second heat-treatment cycles before welding. The change in the γ′-phase morphology from cubic to spherical and the increase in particle size of the γ′ phase reduced the hardness of the heat-treated coupons. The type and interaction of precipitates and dislocations determine the degree of hardness in superalloys. The slipping of dislocations occurs through the passage from coarse precipitates and slices of fine γ′ precipitates. Thus, achieving the optimum size of precipitates will result in the maximum hardness in the base metal. Therefore, with increasing size of the precipitates in the coupons subjected to the second heat-treatment cycle, a decrease in the hardness value is observed.

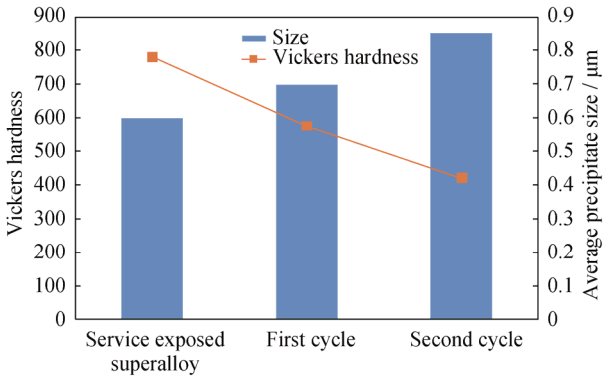

Fig. 7. Hardness variations and the particle size of γ′ precipitates of coupons subjected to the two heat-treatment cycles.

3.2. Post-weld microstructure

Fig. 8 shows optical microscopy images of the microstructure in three different sections of the welded coupon subjected to the first heat-treatment cycle. Cracking is clearly observed as a centerline crack that reached the surface of the weld metal. This crack was formed because of a continuous boundary

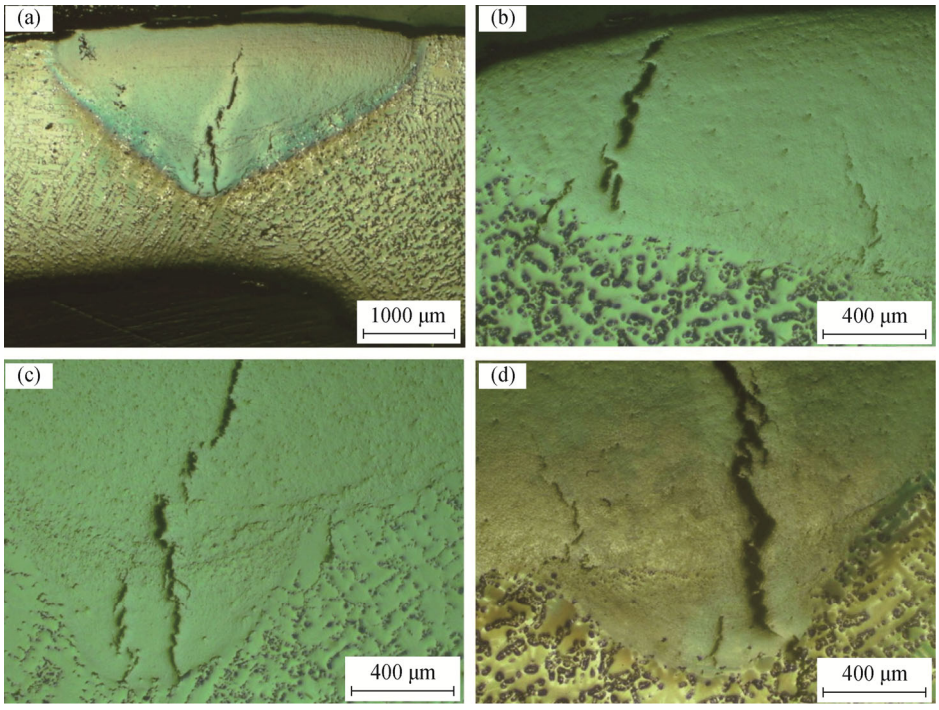

Fig. 8. Optical microscopy images of the first cross section (a, c), the second cross section (b), and the third cross section (d) of the welding part which formed liquation cracks during the first heat-treatment cycle.

formed alongside the center of the weld bead with high heat input and at a high welding travel speed. Under these conditions, a large columnar structure is formed in the width of the bead and large amounts of eutectic and brittle phases form along the central line. This segregation leads to the melting of these areas from the bead during the first heat treatment or under the high-temperature conditions that cause crack formation [16]. Several examples of liquation cracks are observed in the HAZ region. These cracks originated from the grain boundary of the metal and extended along the boundary to the weld metal.

Liquation cracks that formed in the HAZ (Fig. 9(a)) are attributed to metallurgical changes that occurred in the HAZ because of the melting of microstructure components such as eutectic and MC carbides. During rapid heating in the EBW process, these phases on the grain boundary often cannot be completely dissolved in the matrix phase; thus, a eutectic phase with a low melting point and a liquation surrounding the grain boundary are formed. The liquid film formed on the boundary in the HAZ region is solidified again, and this film is debonded from the matrix; it therefore cannot withstand the tensile stresses created at the end of the weld bead, resulting in the formation of these types of cracks. The formation of a crack in the MC carbide neighborhood is shown in Fig. 9(a). The nucleation and growth of this crack is the result of the liquation and re-solidification of the carbide phase in the crack neighborhood.

The results of the EDS analysis at point A in Fig. 9(a) and the distribution of the Nb, Ti, and W elements are presented in Table 4 and Fig. 9, respectively. These results clearly demonstrate that this crack forms because of the melting of an MC-type carbide that is rich in tungsten, titanium, and niobium (Fig. 9). These results demonstrate the destructive role of grain-boundary strengthening phases (e.g., MC-rich carbides of tungsten and niobium) in the welding of ZhS6U superalloys.

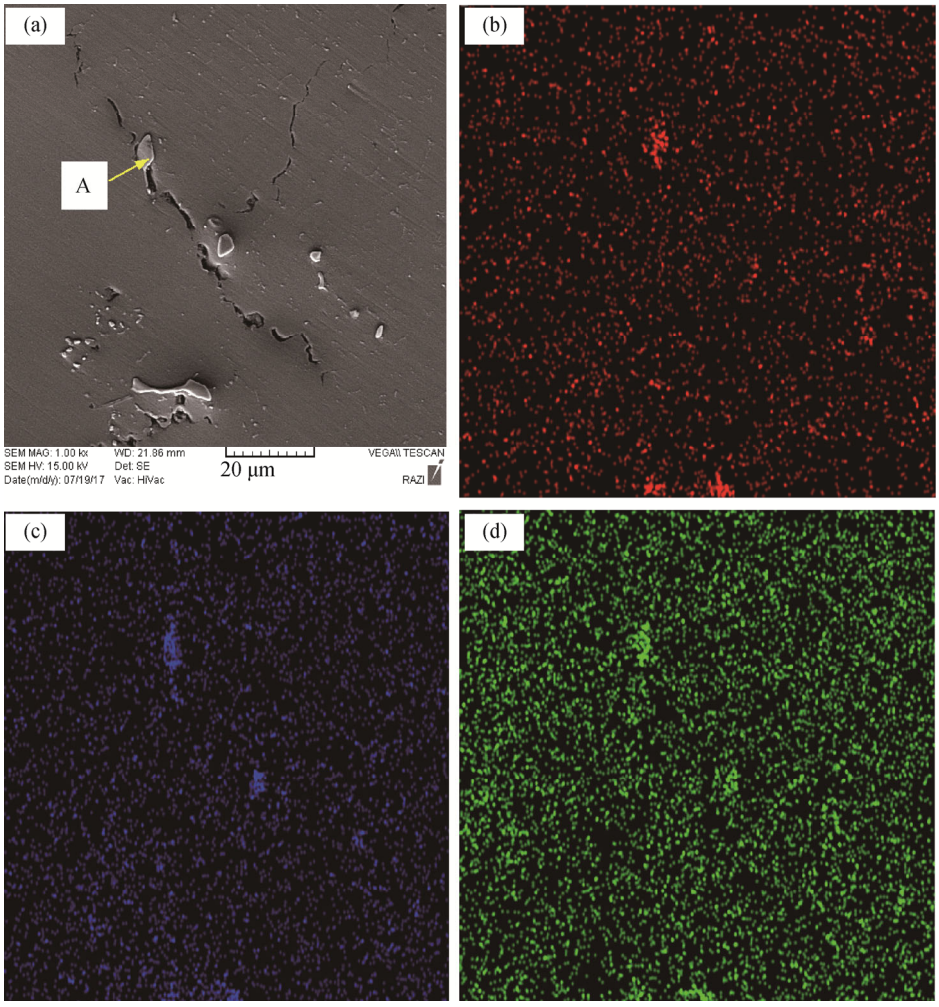

Fig. 9. Liquation crack image microstructure (a) and maps of the element distribution of Nb (b), Ti (c), and W (d).

Table 4. EDS analysis results for point A in Fig. 9 at%

C	Nb	Ti	W	Mo	Cr	Ni
38.7	14.1	31.9	7.6	3.8	1.8	2.1

During the fusion welding of nickel-based superalloys, the eutectic and carbide phases on the boundary in the HAZ will be exposed to the heat of welding, and these phases should be dissolved into the matrix phase. The rapid heating of the EBW process causes incomplete dissolution of eutectic phases in the matrix phase and forms a eutectic phase with a low melting point, resulting in melting of a portion of the surrounding grain boundary.

A lack of sufficient penetrating of the main elements of the carbide-forming phase leads to the formation of low-temperature and re-solidified phases in the HAZ. The tensile stresses caused by the welding process will lead to phase separation from the matrix and the formation of liquation cracks.

To compare the contents of the soluble elements in regions of the HAZ that are liquated and the contents of these elements in the γ matrix, we performed line chemical analysis along the liquation crack (Fig. 10). The variation of the soluble elements along this line indicates higher contents of Ti, Nb, and W in the melting phase around the crack compared with the contents of these elements in the matrix, which confirms the incomplete dissolution of the phases around the crack liquation.

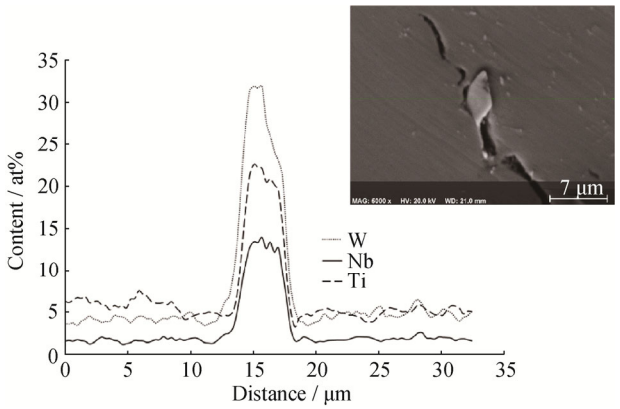

Fig. 10. Line chemical analysis along the liquation crack interrupt.

The interface between the weld region and the base metal after the second heat-treatment cycle is shown in Fig. 11. The welding region with an equiaxed grain and fine dendritic structures is free from any solidification and liquation cracks. No liquation cracking was observed in the HAZ of the welded coupon after the second pre-weld heat-treatment cycle.

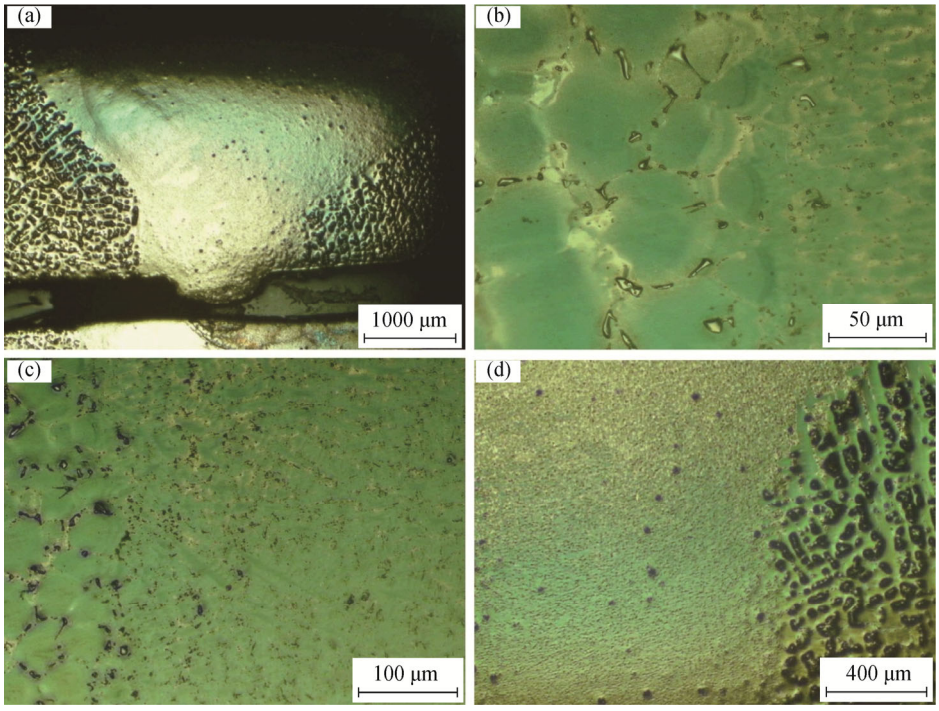

Fig. 11. Optical microscopy images of the welded part subjected to the second heat-treatment cycle at different magnifications.

The thermal stresses caused by welding are strongly dependent on the ability of the base alloy to release the thermal stresses created during cooling. This ability is directly related to the hardness of the base alloy prior to the welding process. The base-metal superalloy with high hardness after welding exhibits greater resistance to stress relaxation. The base metal

forces higher welding stresses to the HAZ that is heated and re-solidified. These weak areas in the HAZ cannot withstand tension; thus, liquation cracks form in the HAZ. By contrast, the low-hardness base superalloy has greater ability to release welding stresses and forces less stress on weakened areas in the HAZ.

The high hardness of the welded coupons subjected to the first heat-treatment cycle leads to a greater stress concentration in the HAZ, which promotes the formation of liquation cracks in the HAZ and creates large free-solidification cracks in the weld region of the coupons subjected to the first heat-treatment cycle. However, the hardness of the coupon subjected to the second heat-treatment cycle was reduced to a desirable value to enable the release of tensile stresses. The weldments were therefore free of any defects and cracks.

In addition to the solidification and liquation cracking, microstructural evolution of the fusion zone was studied. The fusion zones of both welded samples have similar microstructural constituents. The microstructure of the fusion zone was composed of three parts: the matrix, eutectic, and the carbide phase regions. Fig. 12 shows the fusion-zone microstructure of samples subjected to the second pre-weld heat-treatment cycle. Very fine and spheroidal γ′-precipitates formed in the matrix of the fusion zone, with an average size of 20 to 60 nm. These precipitates nucleated during the solidification stage of the EBW process with a high cooling rate; the growth rate of the γ′ phase was very low.

Fig. 12. Microscopic image of the fusion zone of the sample subjected to the second heat-treatment cycle.

4. Conclusions

(1) The different morphologies and sizes of the γ′ precipitates formed during the pre-welding heat-treatment cycles changed the ability to release the tensile stresses caused by the matrix phase cooling after EBW.

(2) The high hardness in the welded coupons after the first heat-treatment cycle resulted in greater resistance to stress release by the base alloy, and the concentration of stress in the base metal was responsible for the formation of liquation cracks in the HAZ and the solidification cracks in the weld area.

(3) The hardness of the welded coupons subjected to the second heat-treatment cycle was sufficiently reduced to enable the release of tensile stresses caused by cooling after EBW; the weld region was consequently free of any welding defects and cracks.

Acknowledgements

The authors would like to express their appreciation for Mr. Mehdi Talebipoor's support in this research for the provision of alloys and other laboratory equipment.

References

[1] M.A. Godovanets, B.A. Prusakov, and I.I. Lysenko, Regenerative heat treatment of blades of high-temperature nickel alloys, *Met. Sci. Heat. Treat*., 38(1996), No. 5, p. 202.

[2] M.F. Chiang and C. Chen, Induction-assisted laser welding of IN-738 nickel-base superalloy, *Mater. Chem. Phys.*, 114(2009), No. 1, p. 415.

[3] A.T. Egbewande, R.A. Buckson, and O.A. Ojo, Analysis of laser beam weldability of Inconel 738 superalloy, *Mater. Charact.*, 61(2010), No. 5, p. 569.

[4] Y. Danis, C. Arvieu, E. Lacoste, T. Larrouy, and J.M. Quenisset, An investigation on thermal, metallurgical and mechanical states in weld cracking of Inconel 738LC superalloy, *Mater. Des.*, 31(2010), No. 1, p. 402.

[5] M. Montazeri and F.M. Ghaini, The liquation cracking behavior of IN738LC superalloy during low power Nd:YAG pulsed laser welding, *Mater. Charact.*, 67(2012), p. 65.

[6] M. Prager, *Welding of Precipitation-Hardening Nickel-Base Alloys*, Welding Research Council, New York, 1968.

[7] H.A. Shahsavari, A.H. Kokabi, and S. Nategh, Effect of pre-weld microstructure on HAZ liquation cracking of Rene 80 superalloy, *Mater. Sci. Technol.*, 23(2007), No. 5, p. 547.

[8] O.A. Ojo, Intergranular liquation cracking in heat affected zone of a welded nickel based superalloy in as cast condition, *Mater. Sci. Technol.*, 23(2007), No. 10, p. 1149.

[9] T. Böllinghaus, H. Herold, C.E. Cross, and J.C. Lippold, *Hot Cracking Phenomena in Welds II*, Springer, Berlin, 2008.

[10] M. Qian and J.C. Lippold, The effect of annealing

twin-generated special grain boundaries on HAZ liquation cracking of nickel-base superalloys, *Acta Mater.*, 51(2003), No. 12, p. 3351.

[11] O.A. Ojo, N.L. Richards, and M.C. Chaturvedi, Contribution of constitutional liquation of gamma prime precipitate to weld HAZ cracking of cast Inconel 738 superalloy, *Scripta Mater.*, 50(2004), No. 5, p. 641.

[12] O.A. Ojo, N.L. Richards, and M.C. Chaturvedi, Microstructural study of weld fusion zone of TIG welded IN 738LC nickel-based superalloy, *Scripta Mater*., 51(2004), No. 7, p. 683.

[13] J.M. Kalinowski, *Weldability of a Nickel-Based Superalloy*, NASA Contractor Report 195376, 1994.

[14] V.M. Polyanskii, V.V. Gavrilyuk, V.Z. Zagorskii, A.V. Logunov, A.M. Polyanskii, and M.I. Silis, Structure, properties, and fracture mechanism of cast refractory nickel alloy, *Met. Sci. Heat Treat*., 46(2004), No. 9-10, p. 392.

[15] M.J. Donachie and S.J. Donachie, *Superalloys: A Technical Guide*, 2nd Ed., ASM International, Ohio, 2002.

[16] O. Hunziker, D. Dye, and R.C. Reed, On the formation of a centreline grain boundary during fusion welding, *Acta Mater.*, 48(2000), No. 17, p. 4191.